# A simulation of convective dynamo in the solar convective envelope: maintenance of the solar-like differential rotation and emerging flux

Yuhong Fan and Fang Fang

*High Altitude Observatory, National Center for Atmospheric Research, 3080 Center Green Drive, Boulder, CO 80301*

## ABSTRACT

We report the results of a magneto-hydrodynamic (MHD) simulation of a convective dynamo in a model solar convective envelope driven by the solar radiative diffusive heat flux. The convective dynamo produces a large-scale mean magnetic field that exhibits irregular cyclic behavior with oscillation time scales ranging from about 5 to 15 years and undergoes irregular polarity reversals. The mean axisymmetric toroidal magnetic field is of opposite signs in the two hemispheres and is concentrated at the bottom of the convection zone. The presence of the magnetic fields is found to play an important role in the self-consistent maintenance of a solar-like differential rotation in the convective dynamo model. Without the magnetic fields, the convective flows drive a differential rotation with a faster rotating polar region. In the midst of magneto-convection, we found emergence of strong super-equipartition flux bundles at the surface, exhibiting properties that are similar to emerging solar active regions.

*Subject headings:* magnetohydrodynamics(MHD) - Sun: dynamo - Sun: interior

## 1. Introduction

Despite the turbulent nature of solar convection, the sun's large scale magnetic field exhibits remarkable order and organization such as the 11-year sunspot cycle (e.g. Maunder 1922) and the Hale's polarity rule of the bipolar active regions (Hale et al. 1919; Hale & Nicholson 1925). In recent years, global fully dynamic three-dimensional (3D) convective dynamo simulations have been making headway in producing the solar-like cyclic behavior of the large scale magnetic field (e.g. Ghizaru et al. 2010; Racine et al. 2011; Käpylä et al. 2012; Augustson et al. 2013) and the self-consistent formation of buoyant, active region like emerging tubes from dynamo generated strong toroidal fields (Nelson et al. 2011, 2013, 2014).

Most of these simulations have differential rotation with cylindrical iso-rotation contours throughout the convection zone (see review by Charbonneau 2013), and some are considering rotation rate 3 times the solar rate. In this paper we present a convective dynamo simulation driven by the solar radiative diffusive heat flux and maintains a differential rotation profile that resembles more closely to the solar differential rotation in the convection zone in terms of the pole-equator contrast and the more conical iso-contours of rotation in the mid-latitude region. The convective dynamo produces a large-scale mean magnetic field with irregular cyclic behavior and polarity reversals very similar to a convective dynamo presented in Miesch et al. (2011). We demonstrate in this paper the important role the magnetic fields play in the maintenance of the solar-like differential rotation. We also show the emergence of strong super-equipartition flux tubes near the surface that exhibit some properties similar to emerging solar active regions.

## 2. The Numerical Model

We solve the following anelastic MHD equations using a finite-difference spherical anelastic MHD code (Fan 2008; Fan et al. 2013):

$$\nabla \cdot (\rho_0 \mathbf{v}) = 0, \tag{1}$$

$$\rho_0 \left[ \frac{\partial \mathbf{v}}{\partial t} + (\mathbf{v} \cdot \nabla)\mathbf{v} \right] = 2\rho_0 \mathbf{v} \times \boldsymbol{\Omega} - \nabla p_1 + \rho_1 \mathbf{g} + \frac{1}{4\pi}(\nabla \times \mathbf{B}) \times \mathbf{B} + \nabla \cdot \mathcal{D} \tag{2}$$

$$\rho_0 T_0 \left[ \frac{\partial s_1}{\partial t} + (\mathbf{v} \cdot \nabla)(s_0 + s_1) \right] = \nabla \cdot (K\rho_0 T_0 \nabla s_1) - (\mathcal{D} \cdot \nabla) \cdot \mathbf{v} + \frac{1}{4\pi}\eta(\nabla \times \mathbf{B})^2 - \nabla \cdot \mathbf{F}_{\rm rad} \tag{3}$$

$$\nabla \cdot \mathbf{B} = 0 \tag{4}$$

$$\frac{\partial \mathbf{B}}{\partial t} = \nabla \times (\mathbf{v} \times \mathbf{B}) - \nabla \times (\eta \nabla \times \mathbf{B}), \tag{5}$$

$$\frac{\rho_1}{\rho_0} = \frac{p_1}{p_0} - \frac{T_1}{T_0}, \tag{6}$$

$$\frac{s_1}{c_p} = \frac{T_1}{T_0} - \frac{\gamma - 1}{\gamma}\frac{p_1}{p_0}. \tag{7}$$

In the above, $s_0(r)$, $p_0(r)$, $\rho_0(r)$, $T_0(r)$, and $\mathbf{g} = -g_0(r)\hat{\mathbf{r}}$ denote the profiles of entropy, pressure, density, temperature, and the gravitational acceleration of a time-independent, reference state of hydrostatic equilibrium and nearly adiabatic stratification, $c_p$ is the specific heat capacity at constant pressure, $\gamma$ is the ratio of specific heats, and $\mathbf{v}$, $\mathbf{B}$, $s_1$, $p_1$, $\rho_1$, and $T_1$ are the velocity, magnetic field, entropy, pressure, density, and temperature to be solved that describe the changes from the reference state. $\boldsymbol{\Omega}$ denotes the solid body rotation rate

of the Sun and is the rotation rate of the frame of reference, where $\Omega = 2.7 \times 10^{-6}\,\text{rad s}^{-1}$. $\mathcal{D}$ is the viscous stress tensor: $\mathcal{D}_{ij} = \rho_0 \nu \left[ S_{ij} - (2/3)(\nabla \cdot \mathbf{v})\delta_{ij} \right]$, where $\nu$ is the kinematic viscosity, $\delta_{ij}$ is the unit tensor, and $S_{ij}$ is the strain rate tensor given by the following in spherical polar coordinates:

$$S_{rr} = 2\frac{\partial v_r}{\partial r} \tag{8}$$

$$S_{\theta\theta} = \frac{2}{r}\frac{\partial v_\theta}{\partial \theta} + \frac{2v_r}{r} \tag{9}$$

$$S_{\phi\phi} = \frac{2}{r\sin\theta}\frac{\partial v_\phi}{\partial \phi} + \frac{2v_r}{r} + \frac{2v_\theta}{r\sin\theta}\cos\theta \tag{10}$$

$$S_{r\theta} = S_{\theta r} = \frac{1}{r}\frac{\partial v_r}{\partial \theta} + r\frac{\partial}{\partial r}\left(\frac{v_\theta}{r}\right) \tag{11}$$

$$S_{\theta\phi} = S_{\phi\theta} = \frac{1}{r\sin\theta}\frac{\partial v_2}{\partial \phi} + \frac{\sin\theta}{r}\frac{\partial}{\partial \theta}\left(\frac{v_\phi}{\sin\theta}\right) \tag{12}$$

$$S_{\phi r} = S_{r\phi} = \frac{1}{r\sin\theta}\frac{\partial v_r}{\partial \phi} + r\frac{\partial}{\partial r}\left(\frac{v_\phi}{r}\right). \tag{13}$$

$K$ denotes the thermal diffusivity, and $\eta$ is the magnetic diffusivity. In equation (3),

$$\mathbf{F}_{\text{rad}} = -\frac{16\sigma_s {T_0}^3}{3\kappa\rho_0}\frac{dT_0}{dr}\,\hat{\mathbf{r}} \tag{14}$$

is the radiative diffusive heat flux, where $\sigma_s$ is the Stephan-Boltzman constatn, $\kappa$ is the Rosseland mean opacity.

The simulation domain is a partial spherical shell with $r \in [r_i, r_o]$, spanning from $r_i = 0.722R_s$ at the base of the convection zone (CZ) to $r_o = 0.971R_s$ at about 20 Mm below the photosphere, where $R_s$ is the solar radius, $\theta \in [\pi/2 - \Delta\theta, \pi/2 + \Delta\theta]$ with $\Delta\theta = \pi/3$, and $\phi \in [0, 2\pi]$. The domain is resolved by a grid with 96 grid points in $r$, 512 grid points in $\theta$, and 768 grid points in $\phi$. J. Christensen-Dalsgaard's (JCD) solar model (Christensen-Dalsgaard et al. 1996) is used for the reference profiles of $T_0$, $\rho_0$, $p_0$, $g_0$ in the simulation domain. We assumed that $s_0 = 0$ for the reference state. The heating (the last term in eq. [3]) due to the solar radiative diffusive heat flux drives a radial gradient of $s_1$ that drives the convection. We set the thermal diffusivity $K = 3 \times 10^{13}\,\text{cm}^2\,\text{s}^{-1}$, the viscosity $\nu = 10^{12}\,\text{cm}^2\,\text{s}^{-1}$, and the magnetic diffusivity $\eta = 10^{12}\,\text{cm}^2\,\text{s}^{-1}$ at the top of the domain, and they all decrease with depth following a $1/\sqrt{\rho_0}$ profile. The stratification of the domain includes approximately 4 density scale heights between the top and the bottom, and thus the above diffusivities decrease to $K = 4.02 \times 10^{12}\,\text{cm}^2\,\text{s}^{-1}$, $\nu = 1.34 \times 10^{11}\,\text{cm}^2\,\text{s}^{-1}$, $\eta = 1.34 \times 10^{11}\,\text{cm}^2\,\text{s}^{-1}$ at the bottom of the CZ domain. The rationale for our choice of such depth dependent diffusivities for the numerical experiments here is that, if the dominant spatial scales of

convection decreases with height, it may be expected that more heat is transported by the unresolved scales as one moves towards the top of the simulation domain, and hence the greater diffusivities there. Furthermore, with a low magnetic diffusivity and viscosity in the deep CZ, should buoyant magnetic structures develop, they would be able to better preserve their magnetic buoyancy and rise. Given the above diffusivities, the various diffusive time scales for the simulation are estimated as follows. The viscous and magnetic diffusive time scales $(\Delta r)^2/\nu$ and $(\Delta r)^2/\eta$ range from about 71 years near the bottom of CZ to about 10 years near the top, and the thermal diffusive time scale $(\Delta r)^2/K$ ranges from about 2.4 years near the bottom to about 0.3 years near the top, where we have used the depth of the CZ domain $\Delta r$ for the estimate.

We impose $\partial s_1/\partial r = 0$ at the bottom and $s_1 = 0$ at the top boundary. We also impose a latitudinal gradient of entropy at the lower boundary:

$$\left(\frac{\partial s_1}{\partial \theta}\right)_{r_i} = \frac{\pi \Delta s_i}{\Delta \theta} \sin\left(\frac{\pi(\theta - \pi/2)}{\Delta \theta}\right) \tag{15}$$

where $\Delta s_i = 431.4$ erg g$^{-1}$ K$^{-1}$, corresponding to a pole to equator temperature difference of about 6.8 K, to represent the tachocline induced entropy variation that can break the Taylor-Proudman constraint in the CZ (Rempel 2005). At the two $\theta$ boundaries, $s_1$ is assumed symmetric. The velocity boundary condition is non-penetrating and stress free at the top, bottom and the two $\theta$-boundaries. For the magnetic field we assume perfect conducting walls for the bottom and the $\theta$-boundaries and radial field at the top boundary. All quantities are naturally periodic at the $\phi$ boundaries.

For the initial state, we specify the initial $s_1$ such that its horizontal average: $<s_1>_{t=0}$, satisfies:

$$K\rho_0 T_0 \frac{d <s_1>_{t=0}}{dr} = \frac{L_s}{4\pi r^2} - F_{\rm rad}, \tag{16}$$

where $L_s$ is the solar luminosity, $F_{\rm rad}$ is the absolute magnitude of $\mathbf{F}_{\rm rad}$ given in equation (14), and at the lower boundary $r_i$, $L_s/4\pi r^2 = F_{\rm rad}$. Equation (16) lets the initial thermal conduction together with radiative diffusion completely carry the solar luminosity, which sets up an initial unstable entropy gradient $<s_1>_{t=0}$. We start the simulation with a small initial seed magnetic and velocity field and let the magneto-convection evolve to a statistical steady state.

## 3. Results

### 3.1. Overview of the convective dynamo

Figure 1 shows the magnetic and kinetic energies in the statistically steady convective flows in the simulation domain over a time span of about 74 years. The total magnetic energy $E_m$ maintained by the dynamo is about 10% of the total kinetic energy $E_k$ of the convective envelope. The energy of the azimuthally averaged (mean) magnetic field $E_{m,mean}$ only constitutes a small fraction of $E_m$, oscillating from about 1% to 10% of $E_m$.

Figure 2(a) shows the depth variation of the mean entropy gradient established in the CZ domain in the statistical steady state. The entropy gradient reaches a value of about $4.26 \times 10^{-6} \, \mathrm{erg}^{-1}\mathrm{K}^{-1}\mathrm{cm}^{-1}$ at the top boundary at about $0.97 R_s$, which is of a similar order of magnitude as the entropy gradient ($\sim 10^{-5} \, \mathrm{erg}^{-1}\mathrm{K}^{-1}\mathrm{cm}^{-1}$) at this depth in the solar model of JCD. Figure 2(b) shows the various horizontally integrated energy fluxes (normalized to the solar luminosity $L_s$) through the domain as a function of radius established in the statistical steady state. These are respectively, the integrated radiative diffusive heat flux (red curve): $L_{\mathrm{rad}} = 4\pi r^2 F_{\mathrm{rad}}$, the convective enthalpy flux (black curve):

$$L_{\mathrm{conv}} = 4\pi r^2 \rho_0 c_p <v_r T_1> \tag{17}$$

the conductive energy flux by thermal diffusion (yellow curve):

$$L_{\mathrm{cond}} = -4\pi r^2 K \rho_0 T_0 \frac{d <s_1>}{dr}, \tag{18}$$

the kinetic energy flux (blue curve):

$$L_{\mathrm{kin}} = 4\pi r^2 \frac{\rho_0}{2} <v^2 v_r> \tag{19}$$

the viscous energy flux (black dashed curve):

$$L_{\mathrm{vis}} = -4\pi r^2 <v_i \mathcal{D}_{ir}> \tag{20}$$

the Poynting flux (green curve):

$$L_{\mathrm{poyn}} = -4\pi r^2 <\left(\frac{1}{4\pi}(\mathbf{v} \times \mathbf{B}) \times \mathbf{B}\right)_r>, \tag{21}$$

the resistive energy flux (cyan curve):

$$L_{\mathrm{res}} = 4\pi r^2 <\left(\frac{1}{4\pi}(\eta \nabla \times \mathbf{B}) \times \mathbf{B}\right)_r>, \tag{22}$$

and the sum of all the energy fluxes, $L_{\text{tot}}$, is shown as the dash-dotted curve in Figure 2(b). In the above $<>$ denotes averaging over the spherical shell surface and time. The gradual decline of $L_{\text{tot}}$ reflects a numerical deviation from exact energy conservation, which is mainly caused by the numerical diffusion of the magnetic field due to the Alfvén wave-upwind scheme used for advancing the induction equation (Fan 2008; Stone & Norman 1992). This numerical dissipation of magnetic energy is not being put back into the thermal energy in the entropy equation and results in a loss of the total energy, and hence a loss of about 13% of the total energy flux exiting the domain at the top compared to the total energy flux ($L_s$) entering the domain from the bottom. We note that the explicit resistive dissipation of the magnetic field (due to $\eta$), and both the explicit viscous dissipation (due to $\nu$) and the numerical diffusion of momentum are put into the thermal energy in the entropy equation as resistive and viscous heating to maintain energy conservation. From Figure 2, it can be seen that the enthalpy flux of the resolved convection transports about 66% of the solar luminosity in the middle of the CZ, and due to the high thermal diffusivity $K$, thermal conduction also transports a substantial fraction of the solar luminosity (about 36% at the middle of the CZ). The kinetic energy flux of the convective flows is downward and peaks at about 16% of the solar luminosity. The energy fluxes due to the Poynting flux (mostly downward), resistive, and viscous transport are all much smaller.

Figure 2(c) shows the depth variation of the peak downflow (solid black curve), and the r.m.s. speed $v_{\text{rms}}$ (dash-dotted black curve), of the statistical steady convective flows in the domain. Note in computing $v_{\text{rms}}$, we take out the azimuthally averaged velocity components and only sum up the azimuthally fluctuating parts of the velocity components. Also shown are the corresponding magnetic field strength in equipartition with the peak downflow speed (solid red curve) and the r.m.s. speed (dash-dotted red curve). It can be seen that the equipartition field strength $B_{\text{eq}}$ corresponding to the peak down flow speed reaches $\approx 63$ kG, while $B_{\text{eq}}$ corresponding to the r.m.s. speed is $\sim 10$ kG for the deep and mid convection zone, and decrease to about 5000 G near the top boundary at about $r = 0.971 R_s$. Following Käpylä et al. (2012), we compute the following non-dimensional numbers characterizing the convective flows. The Reynolds number $R_e = u_{\text{rms}}/\nu k_f$ ranges from about 130 at the bottom to about 50 at the top, and with a mid convection zone value of about 128, where $k_f = 2\pi/(r_o - r_i)$ and $u_{\text{rms}} = ((3/2) <v_r{}^2 + v_\theta{}^2>)$ is the r.m.s. velocity at each depth omitting the contribution from the azimuthal velocity. The Coriolis number $C_O = (2\Omega/u_{\text{rms,all}} k_f) = 1.3$, where $u_{\text{rms,all}} = ((3/2) <v_r{}^2 + v_\theta{}^2>)$ with the averaging $<>$ done for the entire domain. We can compare the values of these non-dimensional numbers with the corresponding ones in Käpylä et al. (2012): $R_e = 36$ and $C_O = 7.6$. It appears the convective flow in our dynamo simulation is moderately more turbulent as characterized by the larger $R_e$, especially in the deeper layers of the CZ. Our Coriolis number $C_O$ is

significantly lower, indicating that our convective dynamo is operating in a significantly less rotationally dominant regime. If we were to scale their typical r.m.s. velocity to be similar to ours $u_{\mathrm{rms,all}} \approx 100$ m/s, then their $C_O$ would imply a significantly more rapidly rotating stellar envelope (with the solar CZ depth) at about 5 times the solar rotation rate.

Figure 3(a) shows the latitude-time variation of the mean (azimuthally averaged) toroidal magnetic field at a depth near the bottom of the CZ. The mean toroidal magnetic field tends to be of opposite signs for the two hemispheres, and exhibits an irregular cyclic behavior with oscillations of the field strength on time scales ranging from about 5 years to about 15 years and undergoes irregular sign/polarity reversals. The strongest mean toroidal field is concentrated near the bottom of the CZ (see Figure 3(b)), peaking at about 7 kG. Figure 3(c) shows a shell-slice of $B_\phi$ at a depth near the bottom of the CZ, at a cycle maximum phase indicated by the green line in Figure 3(a). It shows that strong toroidal fields $B_\phi$ of a preferred sign (opposite for the two hemispheres) are concentrated in individual channels or filaments in each hemisphere, reaching peak field strength of about 30 kG, which exceeds the field strength in equipartition with the local r.m.s convective speed ($B_{\mathrm{eq}} \approx 13$ kG) but is below the equipartition field strength corresponding to the peak down flow speed ($B_{\mathrm{eq}} \approx 63$ kG). Thus these strong field filaments are not passively advected by convective flows but would be pinned down by the strong down flows if in their paths.

### 3.2. Maintenance of the solar-like differential rotation

Figure 4(a) shows the time and azimuthally averaged rotation rate in the convective envelope self-consistently maintained in the convective dynamo simulation. It shows a solar-like differential rotation profile (e.g. Thompson et al. 2003) with a faster rotation rate at the equator than at the polar region by about 30% of the mean rotation rate, and more conical shaped iso-rotation contours in the mid latitude zone. The time and azimuthally averaged mean meridional flow pattern is shown in Figure 4b in terms of the mass flux function $f$ where $\rho_0 <\mathbf{v}> = \nabla \times [(f/r \sin \theta) \hat{\phi}]$. The meridional circulation has a complex multi-cell structure with a counter-clockwise (clockwise) cell pattern in the low latitude region of the northern (southern) hemisphere, i.e. a poleward near-surface flow in the low latitude region.

Interestingly, we find that the presence of the magnetic field is necessary for the self-consistent maintenance of the solar-like differential rotation profile in the current parameter regime. We have carried out a hydrodynamic simulation (hereafter referred to as the HD case) which is identical to the present convective dynamo simulation except that the magnetic field is set to zero, and found that a very different differential rotation profile (Figure 4(f)) is established in the statistical steady state of the HD simulation. It shows a significantly larger

differential rotation with a faster rotation rate in the polar region than at mid-latitudes and the equator. The iso-rotation contours are also more cylindrical. The meridional flow (Figure 4(g)) shows a more prominent counter-clockwise (clockwise) cell pattern in the northern (southern) hemisphere in the mid depths in the CZ, with much weaker reversed cells in the near surface layer.

To compare the transport of angular momentum in the dynamo and the HD cases, we show in Figures 4(c), 4(d), and 4(e) the meridional profile of the angular momentum flux density in the $r_\perp$ direction (perpendicular to and away from the rotational axis) due respectively to the Reynolds stress of the rotationally influenced convection (panel (c)):

$$RS = \rho_0 r_\perp <v'_{r_\perp} v'_\phi>, \tag{23}$$

the viscous stress (panel (d)):

$$VS = \rho_0 \nu r_\perp (<S_{\phi r}> \sin\theta + <S_{\phi\theta}> \cos\theta), \tag{24}$$

and the Maxwell stress (panel (e)):

$$MS = r_\perp \frac{1}{4\pi} <B_\phi B_{r_\perp}>, \tag{25}$$

where $<>$ denotes time and azimuthal averages and $'$ denotes the azimuthally varying component. The meridional profiles of the angular momentum flux density $RS$ and $VS$ for the corresponding HD case are shown in Figures 4(f) and 4(g). We find that there is a significant difference in the angular momentum flux density by the Reynolds stress between the dynamo and HD cases. The $RS$ for the dynamo case shows an overall more outward transport in its meridional distribution compared to that for the corresponding HD case. Near the lower boundary in the mid latitude range, the presence of the concentrated magnetic field (which helps to damp the convective downflows) results in a more enhanced outward $RS$ flux at the lower boundary layer. The angular momentum flux density $MS$ due to the Maxwell stress in the dynamo case (Figure 4(e)) is found to oppose $RS$, and its strength is the greatest at the lower boundary layer where the magnetic field concentrates. The angular momentum flux density $VS$ simply acts to reduce the differential rotation as expected for both the dynamo and the HD cases. The difference between the dynamo and the HD cases is more clearly seen by evaluating the net angular momentum fluxes in the $r_\perp$ direction integrated over individual concentric cylinders of radii $r_\perp$ centered on the rotation axis, as shown in Figure 5(a) for the dynamo case and Figure 5(b) for the corresponding HD case. It can be seen that the net angular momentum flux due to $RS$ is outward throughout (except near the top boundary) for the dynamo simulation (black curve in Figure 5(a)), which drives a faster rotation in the outer equatorial region. The net angular momentum flux due to $RS$ is

mainly counteracted by the net flux due to $MS$ by the Maxwell stress, with the remaining difference balanced by the significantly smaller net fluxes due to $VS$ and the meridional flow. In contrast, the HD simulation shows a significant inward angular momentum transport due to the Reynolds stress (black curve in Figure 5(b)) across the inner cylinders in the high to mid latitude region. This drives a faster rotation in the polar region. Thus it appears that the presence of the magnetic field alters the convective flows such that the resulting Reynolds stress from the convective motions produces a more outward (away from the rotation axis) net transport of the angular momentum needed to drive a solar-like differential rotation. The Rossby number $R_O = v_{\mathrm{rms,all}}/H_p$ is about 0.74 for the dynamo case and 0.96 for the HD case, where $v_{\mathrm{rms,all}} = 125$ m/s for the dynamo case and 157 m/s for the HD case, is the r.m.s. velocity (with the azimuthally averaged mean flow velocity taken out) averaged over the entire volume, and $H_p$ is the pressure scale height at the bottom of the convection zone. The Rossby number measures the importance of the Coriolis force in the force balance. The lower Rossby number in the dynamo simulation shows that the the magnetic fields suppress the convective motions so that they are more rotationally constrained.

A recent systematic study by Gastine et al. (2014) of rotating stellar convection considering a wide range of models shows that the differential rotation profile transitions from being solar-like, with a faster rotating equator, to being anti-solar, with a faster polar rotation rate, at a value of about 1 for the Rossby number. This result is found to be quite general, independent of the detailed model setup (presence of a magnetic field, thickness of the convective layer, density stratification). Our HD case with $R_O = 0.96$ appears to be very close to the transition, and a reduction of $\sim 23\%$ of the overall r.m.s. velocity and $R_O$ by the presence of the magnetic field in the dynamo case is able to significantly alters the angular momentum transport by the rotationally constrained convection, leading to a transition into the solar-like differential rotation. We note that even though the HD case is quite close to the transition, its anti-solar differential rotation appears to be a stable solution not dependent on the history, i.e. not one of two bistable states (Gastine et al. 2014). We have arrived at the statistically steady HD solution with the anti-solar differential rotation by either starting from the initial setup with a seed velocity field as described in section 2, or by starting from the statistically steady state dynamo solution (for which the differential rotation is solar-like) and zero out the magnetic field. The solar-like differential rotation obtained in the convective dynamo simulation also appears to be a stable solution that is not dependent on the history. The differential rotation at the pole and equator remain statistically steady without exhibiting any systematic drift for the $\gtrsim 74$ year period (comparable to the maximum viscous time scale near the bottom of CZ) we have run after the dynamo solution has reached a statistical steady state. Also as we start the dynamo simulation from the initial setup described in section 2, we find that the convective dynamo goes through

an earlier phase of anti-solar differential rotation (for $\sim 6$ years) before it evolves towards the solar-like differential rotation profile as the mean entropy gradient and the convective energy flux settle down to their statistical steady state. Thus it appears that the solar-like differential rotation is the preferred stable solution in the dynamo case.

The transition to a solar-like differential rotation can alternatively be achieved in the non-magnetic hydro simulations by simply increase the viscosity to reduce $R_O$. We have run another hydrodynamic simulation (hereafter referred to as the HVHD case, meaning "high viscosity hydro") where we increase the viscosity $\nu$ by 5 times (with the same $\rho_0^{-1/2}$ depth dependence) compared to the HD case (or the dynamo case). The resulting r.m.s. velocity of the statistical steady convection reached is $v_{\rm rms,all} = 120 m/s$ and the Rossby number $R_O = 0.71$, much closer to those of the dynamo case. The bottom row panels of Figure 4 show respectively the resulting differential rotation profile (Figure 4(j)), meridional circulation (Figure 4(k)), the angular momentum flux density in the $r_\perp$ direction, $RS$ (Figure 4(l)) due to the Reynolds stress, and $VS$ (Figure 4(m)) due to the viscous stress. The integrated net (outward) angular momentum fluxes across concentric cylinders of radius $r_\perp$ centered on the rotation axis is shown in Figure 5(c). It is found that a solar-like differential rotation profile (Figure 4(j)) with faster rotating equator and with a more conical iso-rotation contours in mid-latitude zones is established, although the contrast of rotation rate between the equator and the polar region is bigger, about 44% of the mean rotation rate (compared to about 32% in the dynamo case). The mean meridional circulation (Figure 4(k)) shows a counter-clockwise (clockwise) cell pattern in the low latitude region of the northern (southern) hemisphere, i.e. a poleward near-surface flow in the low latitude region, similar to the dynamo case (Figure 4(b)). We find that the angular momentum transport in the $r_\perp$ direction due to the Reynolds stress for the HVHD case is very similar to that for the dynamo case, both in the meridional profile of the flux density (Figure 4(l) compared to Figure 4(c)) as well as in the integrated net flux across the constant $r_\perp$ concentric cylinders (Figure 5(c) compared to Figure5(a)). But this similar outward net angular momentum flux by the Reynolds stress is now balanced almost entirely by the transport due to the viscous stress, with the absence of the Maxwell stress which is the major component that balances the angular momentum flux by the Reynolds stress in the dynamo case. The comparison between the dynamo and the HVHD cases suggests an effective role of enhanced viscosity played by the magnetic fields, which (1) suppresses the large scale convective motions such that they are more rotationally constrained (lower $R_O$) to produce an outward transport of the angular momentum by the Reynolds stress, necessary to drive a solar-like differential rotation, and (2) takes up the main role to balance the Reynolds stress transport with the Maxwell stress instead of the viscous stress.

Further in Figure 6 we show the various horizontally integrated energy fluxes through

the domain for the HD case (upper panel) and the HVHD case (lower panel), in comparison with the energy fluxes shown in Figure 2(b) for the dynamo case. It can be seen that the dynamo case and the HVHD case show a similar convective energy flux $L_{\mathrm{conv}}$ (reaching about 66% $L_s$ in the dynamo case and about 60% $L_s$ in the HVHD case). In both the dynamo and the HVHD cases, the downward kinetic energy flux $L_{\mathrm{kin}}$ (reaching about 16% $L_s$ in the dynamo and 10% $L_s$ in the HVHD case) is significantly reduced compared to the HD case (reaching about 45% $L_s$). In fact in the HD case (upper panel in Figure 6), the downward kinetic energy flux is so large that the outward convective energy flux $L_{\mathrm{conv}}$ exceeds the solar luminosity in the middle of the convection zone to counter it. The result here indicate again the similar role played by the magnetic fields and the enhanced viscosity in suppressing the downward convective flows.

### 3.3. Emerging flux

In the convective dynamo, the large-scale mean toroidal field as shown in Figure 3(b) is produced by the latitudinal differential rotation shearing a dipolar poloidal mean field. The reason that the mean toroidal field is concentrated towards the bottom of the CZ is mainly due to a downward advective transport of the magnetic energy in the bulk of the convection zone, as represented by $<v_r(B_\theta{}^2 + B_\phi{}^2)/8\pi>$ shown in Figure 7(a). This causes the distribution of the magnetic energy (for both the mean field and the small scale field) to be strongly concentrated towards the bottom (see Figure 7(b)). The decrease with depth of the magnetic diffusivity $\eta$ would also promote stronger fields towards the bottom but is less important here because of the small magnitude of $\eta$ and the long diffusive time scale: $(\Delta r)^2/\eta \sim 10$ years, using the peak $\eta$ value near the surface and the depth of the CZ domain $\Delta r$. The advective time scale for the downward magnetic energy transport across the convection zone is $\Delta r/u_m \sim 0.5$ year is significantly shorter, where we have used $u_m = <v_r(B_\theta{}^2 + B_\phi{}^2)> / <B_\theta{}^2 + B_\phi{}^2>$ evaluated at the middle of the convection zone as a measure of the transport speed. Thus the advective transport acts more quickly.

In the midst of magneto-convectoin, we find occasional active region like flux emergence events in the top layer of the simulation domain. Such an example is shown in Figure 8, where panels (a), (b), (c), and (d) show respectively snapshots of $B_r$, $B_\phi$, $v_r$ and $v_\phi$ at a constant $r$ slice at the depth of 30 Mm below the photosphere. The location of the emerging bipolar region is indicated by an arrow in the panels. It is characterized by a diverging bipolar pattern in $B_r$ (panel (a)) and the emergence of a strong toroidal field patch reaching a peak field strength of 9800 G (panel (b)) (see also the online movie). The emerging region corresponds to an up flow region in $v_r$ (panel (c)), but the upward velocity is not significantly

different from that of other up flow convective cells. The zonal velocity $v_\phi$ of the emerging region shows a diverging pattern, and when averaged over the emerging region, is $\sim 100$ m/s faster than the mean zonal velocity of that latitude. Figure 8(e) shows the subsurface 3D magnetic field configuration in the convective envelope by showing field lines traced from randomly seeded points throughout the volume. The field lines are colored based on their azimuthal field $B_\phi$ as indicated by the color table. It can be seen that relatively more coherent bundles of strong toroidal flux are embedded in the turbulent magnetic fields. In Figure 8(f), regions of strong field strength where the Alfvén speed ($v_a$) exceeds the r.m.s. convective velocity ($v_{\mathrm{rms}}$) for the corresponding depth is outlined with the equipartition iso-surfaces (with $v_a/v_{\mathrm{rms}} = 1$), which are again colored based on the $B_\phi$ value on the iso-surfaces. There is a systematic preference for these strong flux regions to be green or of negative $B_\phi$ (red or of positive $B_\phi$) in the northern (southern) hemisphere. The arrows in Figures 8(e) and 8(f) mark the toroidal flux bundle with super-equipartition field strength that gives rise to the emerging region.

Figure 9 shows a more zoomed in view of the thermodynamic properties of the emerging region at the same depth as that shown in the upper 4 panels of Figure 8. We see that there is a systematic reduction of density (i.e. buoyant, see Figure 9(b)) and pressure (Figure 9(d)) in the emerging region compared to the surrounding, although the reduction magnitude is rather moderate compared to the fluctuations seen in strong downflow lanes and in strong vertical flux tubes in the downflow lanes. The temperature change in the emerging region compared to the surrounding is smaller, partly due to the large thermal conduction. Averaged over the emerging region (area enclosed in the yellow contour in Figure 9(a), $<\rho_1/\rho_0> \approx -1.6 \times 10^{-5}$, $<p_1/p_0> \approx -1.1 \times 10^{-5}$, and $<T_1/T_0> \approx 0.5 \times 10^{-5}$. It can be seen that the temperature change is relatively small compared to the density and pressure change in the emerging region. This suggests that the buoyancy or reduction in density is mainly due to the reduction in gas pressure provided largely by the presence of the magnetic pressure, instead of mainly due to an increase in temperature. In other words, the buoyancy contribution is more from the magnetic buoyancy than the thermal buoyancy.

As can be seen from Figure 8(e), the emerging flux region is the apex of a roughly east-west oriented (toroidal) super-equipartition flux bundle which remain relatively coherent for some distance, before the two ends connect in complex ways to other flux systems. The following end of the coherent flux bundle extends into the middle of the CZ. The fact that the emerging flux has a prograde zonal speed of $\sim 100$ m/s relative to the mean zonal speed of the latitude indicates that it is not a toroidal flux tube rising in isolation from the bottom of the CZ. Because if it were it would have a retrograde flow due to angular momentum conservation as is found in many previous studies of isolated rising flux tubes in the rotating solar CZ (e.g. Caligari et al. 1995; Fan 2008, 2009). The emerging flux bundle must have

well mixed with the local plasma through reconnections, and is continually sheared and amplified by the differential rotation and the local flows against resistive dissipation. The sequence of images in Figure 10 show the sub-surface development of the super-equipartition emerging flux bundle (marked by the arrow) over a 9 day period prior to the time of the flux emergence event shown in Figure 8. It shows that local shear in the upper convection zone contributes significantly to the development of the emerging flux bundle. The left column images show iso-volumes of super-equipartition fields with the surface of the volume colored by $B_\phi$. The right column images show representative field lines traced from the iso-volume corresponding to the emerging flux bundle. It can be seen that a segment of a super-equipartition flux bundle in the middle of the convection zone is sheared and stretched in the prograde direction into a hairpin turn with the upper side of the hairpin forming the emerging flux bundle reaching the top boundary.

We have done a statistical study of the super-equipartition emerging fields. For a time period of about 1 year centered at the cycle maximum phase (green line in Figure 3(a)) and at an interval of 12 hours, we find in the shell slice at 30 Mm depth all the area where the emerging horizontal field exceeds $\sqrt{2}$ times the field strength in equipartition with the r.m.s. convective velocity of that depth. For each pixel (or grid point) of the selected emerging field area, we compute a tilt angle of the horizontal field vector based on the local $B_\phi$ and $B_\theta$. The resulting tilt angle distribution of all the pixels is shown in Figure 11. The quadrant of the tilt angle is such that, if the sign of the azimuthal field $B_\phi$ is consistent with Hale's polarity rule of the cycle, i.e. negative (positive) in the northern (southern) hemisphere, then the tilt angle falls in quadrants I and IV. If the horizontal field vector is tilted clockwise (anti-clockwise) from the cycle preferred azimuthal field direction in the northern (southern) hemisphere by an acute angle, consistent with the mean tilt of solar active regions, then the tilt angle falls in quadrant I. We find from Figure 11 that there is a preference for Hale's polarity rule for the emerging azimuthal field by a ratio of 2.4 to 1 in the area. For those pixels satisfying Hale's rule the mean tilt angle is 7.5°, with an estimated uncertainty of 1.6°. Thus the super-equipartition emerging fields have a statistically significant mean tilt similar to the active region mean tilt (e.g. Stenflo & Kosovichev 2012).

## 4. Discussions

We have presented a 3D convective dynamo driven by the solar radiative diffusive heat flux in the solar CZ, and with a latitudinal gradient of entropy imposed at the bottom, representing the tachocline induced thermal variation that can break the Taylor-Proudman constraint in the CZ (Rempel 2005). The convective dynamo produces a large scale mean

field that undergoes irregular cycles and polarity reversals, and self-consistently maintains a solar-like differential rotation with faster rotation at the equator than at the polar region by about 30% and more conical iso-rotation contours in mid latitudes (e.g. Thompson et al. 2003).

The irregular cyclic behavior of the mean field in our model differs from those in the literature (e.g. Ghizaru et al. 2010; Racine et al. 2011; Käpylä et al. 2012). By comparing the Reynolds number $R_e$ and the Coriolis number $C_O$ (as defined in Käpylä et al. (2012)) achieved in our dynamo run with those of the cyclic dynamo simulation presented in Käpylä et al. (2012) (see section 3.1), we find that their convective dynamo is operating in a significantly more rotationally constrained regime, with their $C_O$ being about 5 times ours. Our convective flows appear to be only moderately more turbulent compared to theirs as reflected in the similar order of magnitude for the $R_e$ values. If we consider our convective r.m.s. velocity to be similar to theirs, then their dynamo would be effectively operating in a stellar envelope that is rotating at about 5 times the solar rotation rate. This is probably the main reason we obtain a very different mean field dynamo behavior compared to that of Käpylä et al. (2012). Our irregularly cycling convective dynamo model also differs significantly in many ways from the cyclic convective dynamo model described in Ghizaru et al. (2010); Racine et al. (2011). Their dynamo model used an implicit large eddy code with no explicit viscosity, magnetic diffusion, and thermal diffusion. But our convective dynamo appears to be operating in a more turbulent regime if we compare the convective downflow speed obtained: about 25 m/s at $r = 0.954R_s$ in (Ghizaru et al. 2010) vs. our $\sim 300$ m/s at the same depth. Given that both models use the solar rotation rate for the convective envelope, this suggests that their dynamo model is also operating in a significantly more rotationally constrained regime with a significantly lower Rossby number compared to ours. The Newtonian cooling treatment of the entropy equation used in Ghizaru et al. (2010); Racine et al. (2011) is very different from our treatment of the energy transport which forces the solar luminosity through the convective domain. Furthermore, their model includes a sub-adiabatically stratified overshoot layer at the bottom of the convection zone which our model does not have. All these contribute to the significant differences in the resulting dynamo behavior.

In both Käpylä et al. (2012) and Racine et al. (2011), because of the significantly higher $C_O$ or lower $R_O$, the convective flows in their corresponding hydro cases in the absence of the magnetic fields are already driving a solar-like differential rotation, and the addition of the magnetic fields in their dynamo cases appear to mainly reduce the differential rotation (Charbonneau 2013). On the other hand for our convective dynamo in a significantly less rotationally constrained regime with $R_O$ closer to 1, the presence of the magnetic field is found to play an important role for the maintenance of the solar-like differential rotation, without which a faster rotating polar region results, as is shown with the corresponding

HD simulation. A solar-like differential rotation profile can alternatively be achieved in the hydro case by increasing the viscosity as shown in the HVHD simulation. The comparison between the dynamo case and the HVHD case indicate that in several aspects the magnetic field plays an effective role of enhanced viscosity to (1) suppress the large scale convective motions such that they become more rotationally constrained to produce an outward transport of angular momentum by the Reynolds stress needed to drive a solar-like differential rotation, (2) take up the main role of balancing the Reynolds stress transport with the Maxwell stress transport instead of the viscous stress under low viscosity conditions, and (3) reduce the downward kinetic energy energy flux. Our resulting differential rotation self-consistently maintained in the convective dynamo simulation is in fairly good agreement with the observed solar differential rotation in both the pole-equator contrast and also the more conical shaped iso-rotation contours in the mid-latitude zone. The more conical iso-rotation contours are achieved by the latitudinal gradient of entropy imposed at the lower boundary as has been described in Rempel (2005); Miesch et al. (2006). The latitudinal gradient of entropy is spread into the bulk of the CZ due to the large thermal diffusivity, and this latitudinal gradient in the CZ provides the necessary balance in the $\phi$ component of the vorticity equation to allow for a non-cylindrical differential rotation to be established (Rempel 2005). Thus the role of the imposed latitudinal entropy gradient is to change the shape of the iso-rotation contours from cylindrical to more conical. It is not the reason for the change of differential rotation from anti-solar (fast rotating pole) to solar-like (faster equator) between the HD and the magnetic cases, both of which have the same latitudinal entropy gradient imposed. That change is brought about by the change in the direction of Reynolds stress transport of the angular momentum.

The large scale mean toroidal field, antisymmetric with respect to the equator, is concentrated at the bottom of the CZ, unlike many of the recent convective dynamo simulations with cylindrical iso-rotation contours and significantly faster (than solar) rotation rates (e.g. Nelson et al. 2013; Augustson et al. 2013), where strong wreath like toroidal field structures are present in the equatorial region of the bulk of the CZ. In the 3D magnetic field of the present simulation (Figure 8), occasional more coherent toroidal flux bundles of super-equipartition field strength are embedded in the turbulent small scale fields, as discussed in section 3.3. Some of these super-equipartition flux bundles rise to the surface to produce active region like flux emergence events. Although these emerging flux bundles show significant magnetic buoyancy, they are not flux bundles rising in isolation from the bottom of the CZ, but are product of continued reconnection and shear amplification by local flows in the CZ. There is a preference for the azimuthal field in the strong emerging field regions to conform to Hale's polarity rule by a ratio of 2.4 to 1 in area, and a statistical significant mean tilt angle of $7.5° \pm 1.6°$ for the emerging horizontal fields, consistent with the active

region mean tilt. However, the violation from Hale's rule is far greater than that of solar active regions. This is because of the very weak mean field component ($\sim 5\%$ of the total magnetic energy) in the current convective dynamo. It is very likely that our dynamo model is still significantly over-estimating the giant-cell convective speed (Hanasoge et al. 2012) and the Sun's dynamo is operating in a significantly more rotationally constrained regime. This is indicated by the more rotationally constrained convective dynamo models of Käpylä et al. (2012); Augustson et al. (2013), which are able to achieved a more regular, solar cycle like cyclic behavior and stronger mean field by effectively increasing the rotation rate. With a significantly lower magnetic diffusion (than have been achieved by current global convective dynamo models), the solar dynamo may be operating in a significantly stronger field regime with a much more suppressed giant-cell convection, and lower Rossby number. This may lead to a stronger Reynolds stress transport of angular momentum that needs to be balanced by a stronger Maxwell's stress and hence the generation of a stronger mean field. But the question remains in regard to how such suppressed convective flows transport the solar luminosity through the CZ, although the convective energy transport in the more magnetic buoyancy dominated regime may be quite different. Furthermore, the inclusion of an overshoot layer below the base of the CZ may be important for the operation of the solar cycle dynamo. The convective dynamo model of Ghizaru et al. (2010); Racine et al. (2011) has achieved a much stronger large scale mean field component, with the mean field magnetic energy comparable to that of the small scale magnetic energy during cycle maxima (compared to the 10% in our model), by allowing penetration and storage of the strong mean field in the stable overshoot layer.

## REFERENCES

Augustson, K., Brun, A. S., Miesch, M. S., & Toomre, J. 2013, ArXiv e-prints

Caligari, P., Moreno-Insertis, F., & Schüssler, M. 1995, ApJ, 441, 886

Charbonneau, P. 2013, Journal of Physics Conference Series, 440, 012014

Christensen-Dalsgaard, J., Dappen, W., Ajukov, S. V., et al. 1996, Science, 272, 1286

Fan, Y. 2008, ApJ, 676, 680

—. 2009, Living Reviews in Solar Physics, 6, 4

Fan, Y., Featherstone, N., & Fang, F. 2013, ArXiv e-prints

Gastine, T., Yadav, R. K., Morin, J., Reiners, A., & Wicht, J. 2014, MNRAS, 438, L76

Ghizaru, M., Charbonneau, P., & Smolarkiewicz, P. K. 2010, ApJ, 715, L133

Hale, G. E., Ellerman, F., Nicholson, S. B., & Joy, A. H. 1919, ApJ, 49, 153

Hale, G. E., & Nicholson, S. B. 1925, ApJ, 62, 270

Hanasoge, S. M., Duvall, T. L., & Sreenivasan, K. R. 2012, Proceedings of the National Academy of Science, 109, 11928

Käpylä, P. J., Mantere, M. J., & Brandenburg, A. 2012, ApJ, 755, L22

Maunder, E. 1922, Mon. Not. R. Astron. Soc., 82, 534

Miesch, M. S., Brown, B. P., Browning, M. K., Brun, A. S., & Toomre, J. 2011, in IAU Symposium, Vol. 271, IAU Symposium, ed. N. H. Brummell, A. S. Brun, M. S. Miesch, & Y. Ponty, 261–269

Miesch, M. S., Brun, A. S., & Toomre, J. 2006, ApJ, 641, 618

Nelson, N. J., Brown, B. P., Brun, A. S., Miesch, M. S., & Toomre, J. 2011, ApJ, 739, L38

—. 2013, ApJ, 762, 73

Nelson, N. J., Brown, B. P., Sacha Brun, A., Miesch, M. S., & Toomre, J. 2014, Sol. Phys., 289, 441

Racine, É., Charbonneau, P., Ghizaru, M., Bouchat, A., & Smolarkiewicz, P. K. 2011, ApJ, 735, 46

Rempel, M. 2005, ApJ, 622, 1320

Stenflo, J. O., & Kosovichev, A. G. 2012, The Astrophysical Journal, 745, 129

Stone, J. M., & Norman, M. L. 1992, ApJS, 80, 791

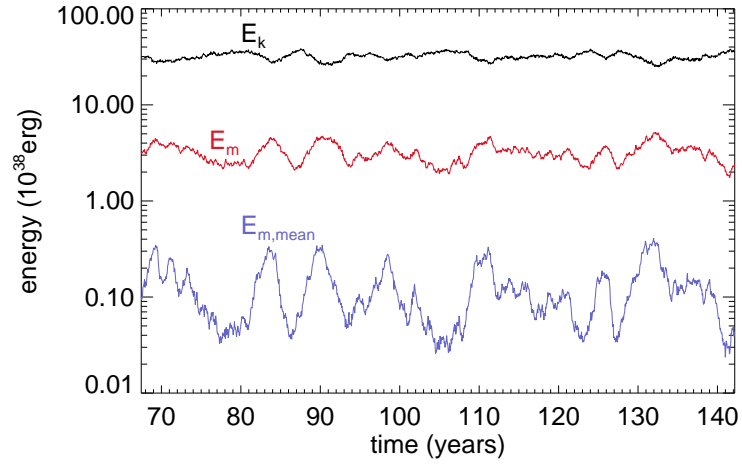Thompson, M. J., Christensen-Dalsgaard, J., Miesch, M. S., & Toomre, J. 2003, ARA&A, 41, 599

Fig. 1.— The temporal variation of the total kinetic energy ($E_k$), total magnetic energy ($E_m$), and the azimuthally averaged mean magnetic field energy ($E_{m,mean}$) of the statistically steady convective flows in the simulation domain.
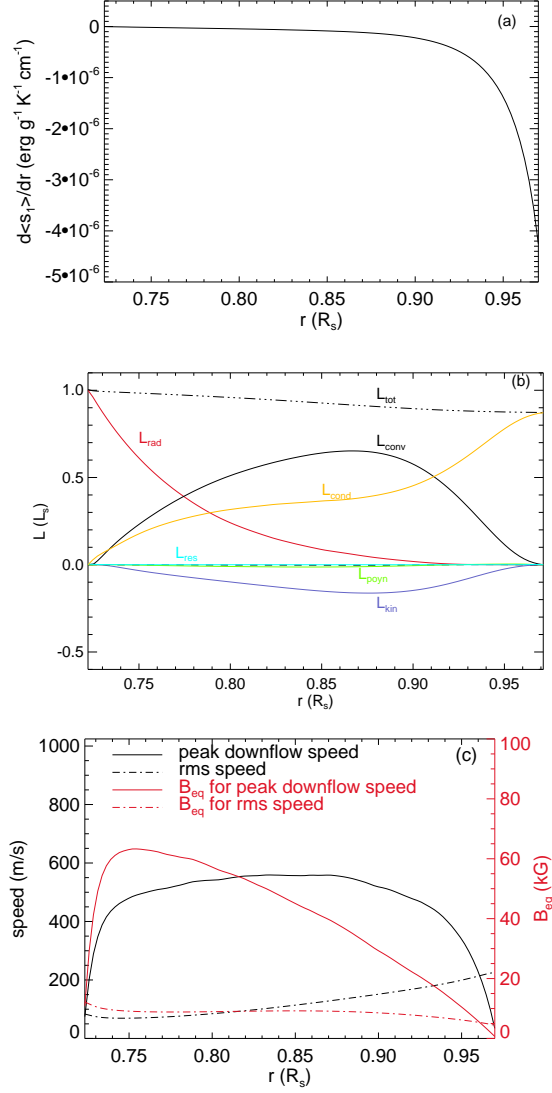
Fig. 2.— Mean profiles established in the statistical steady state of the dynamo simulation: (a) shows the depth variation of the mean entropy gradient; (b) shows the horizontally integrated energy fluxes due to respectively, radiative diffusion $L_{\rm rad}$ (red curve), convection $L_{\rm conv}$ (black curve), thermal conduction $L_{\rm cond}$ (yellow curve), kinetic energy flux $L_{\rm kin}$ (blue curve), viscous flux $L_{\rm vis}$ (dashed line), Poynting flux $L_{\rm poyn}$ (green curve), resistive flux $L_{\rm res}$ (cyan curve), and the sum of all $L_{\rm tot}$ (dash-dotted black curve), as a function of depth (see text for the expressions of $L_{\rm rad}$, $L_{\rm conv}$, $L_{\rm cond}$, $L_{\rm kin}$, $L_{\rm vis}$, $L_{\rm poyn}$, and $L_{\rm res}$); (c) shows the peak downflow and the RMS convective speeds and their corresponding equipartition magnetic field strenghs.
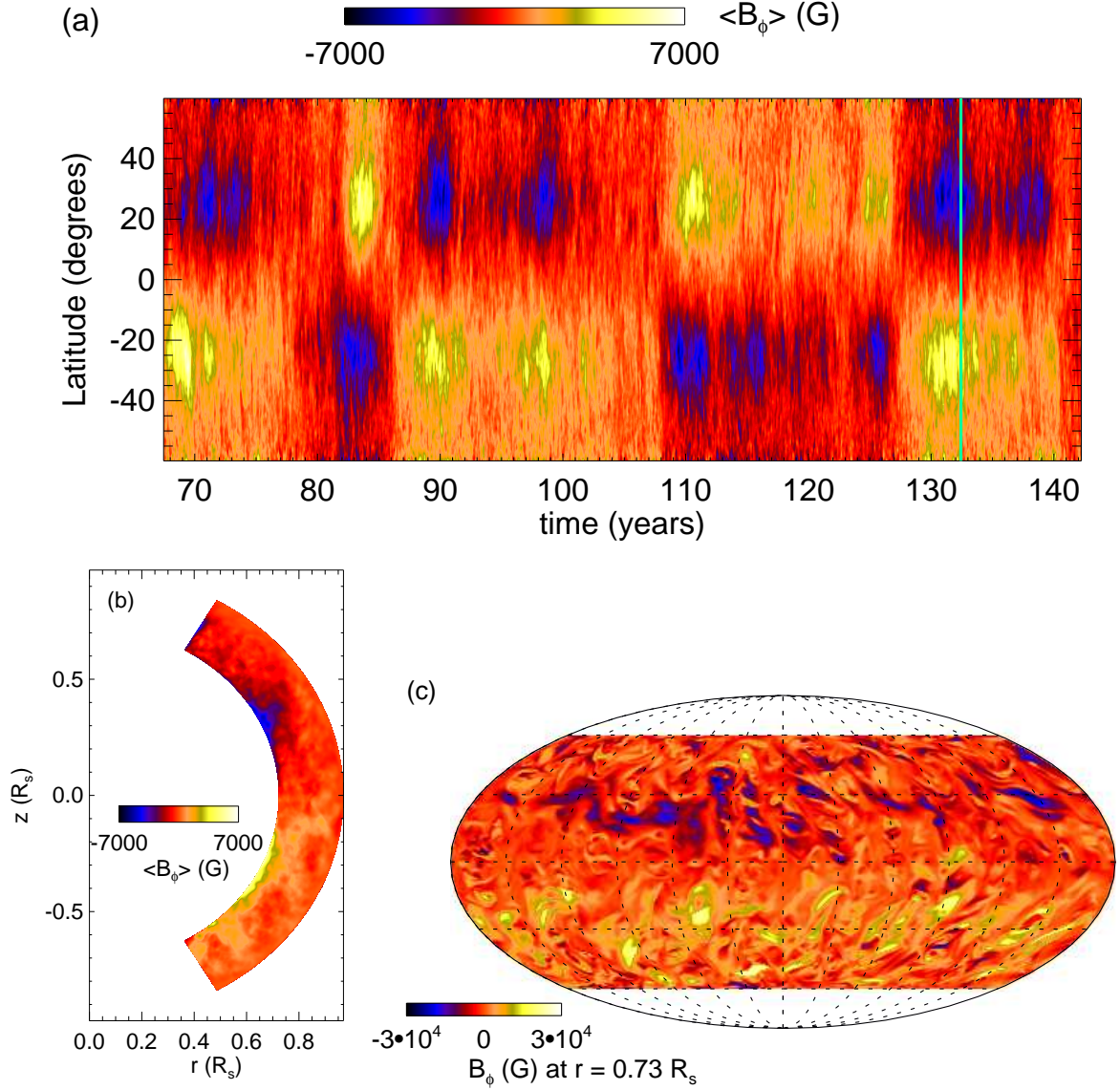
Fig. 3.— (a) The latitude-time variation of the mean (azimuthally averaged) toroidal magnetic field at a depth ($r = 0.73R_s$) near the bottom of the CZ. (b) Azimuthally averaged toroidal magnetic field distribution in the meridional plane at the time marked by the green line in panel (a). (c) A shell slice of the toroidal magnetic field at a depth ($r = 0.73R_s$) near the bottom of the CZ at the same time marked by the green line in panel (a).
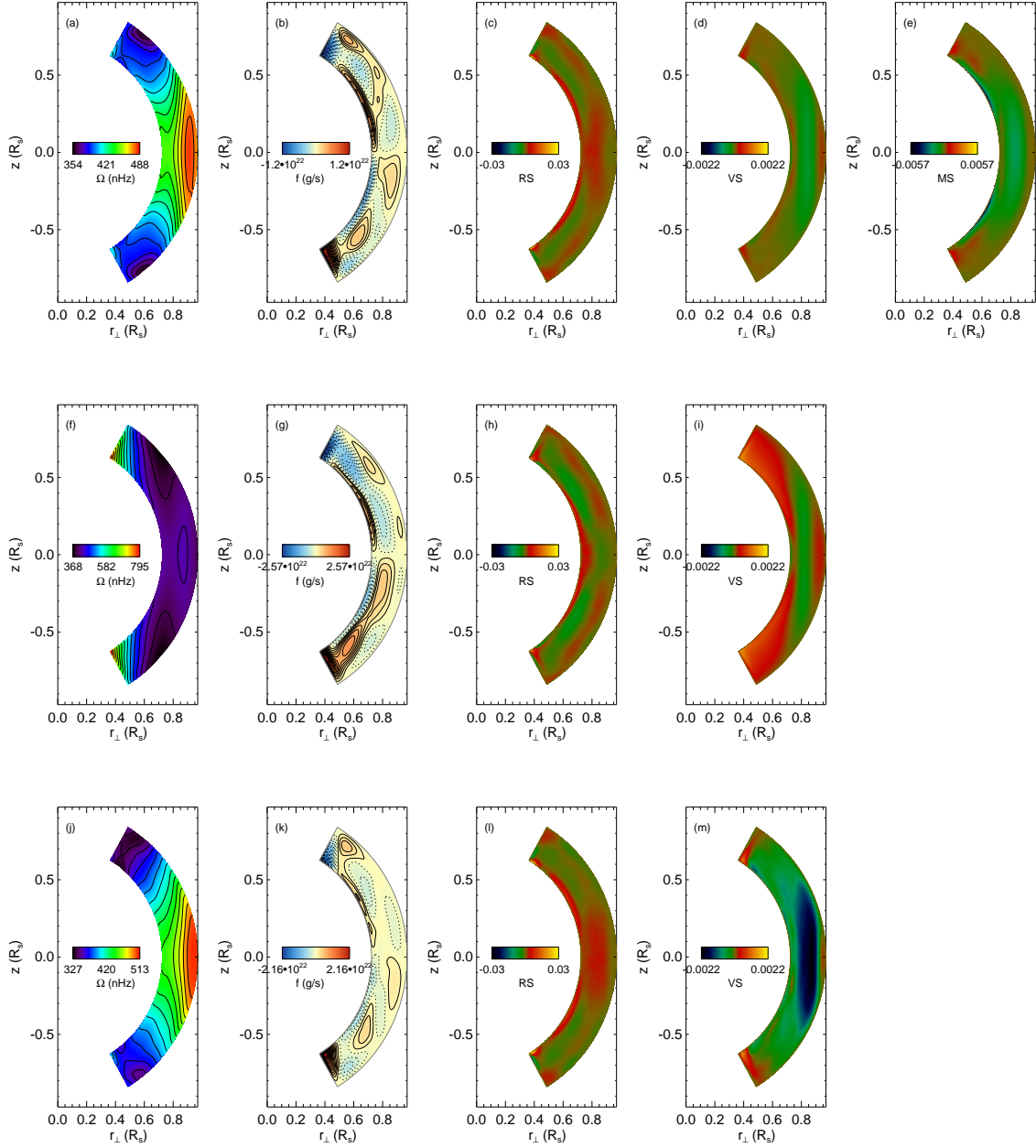
Fig. 4.— Top row panels from left to right show the time and azimuthally averaged mean meridional profile of angular velocity (a), meridional flow mass flux (b), angular momentum flux density in the $r_\perp$ direction due to the Reynolds stress (c), the viscous stress (d), and the Maxwell stress (e) resulting from the dynamo simulation. Middle row panels from left to right show the same as those of the top row except for the results from the corresponding HD simulation and there is not a panel for the Maxwell stress. Bottom row panels from left to right show the same as the middle row, except for the results from the HVHD simulation. See text for the expressions for the various angular momentum flux density RS, VS, and MS.
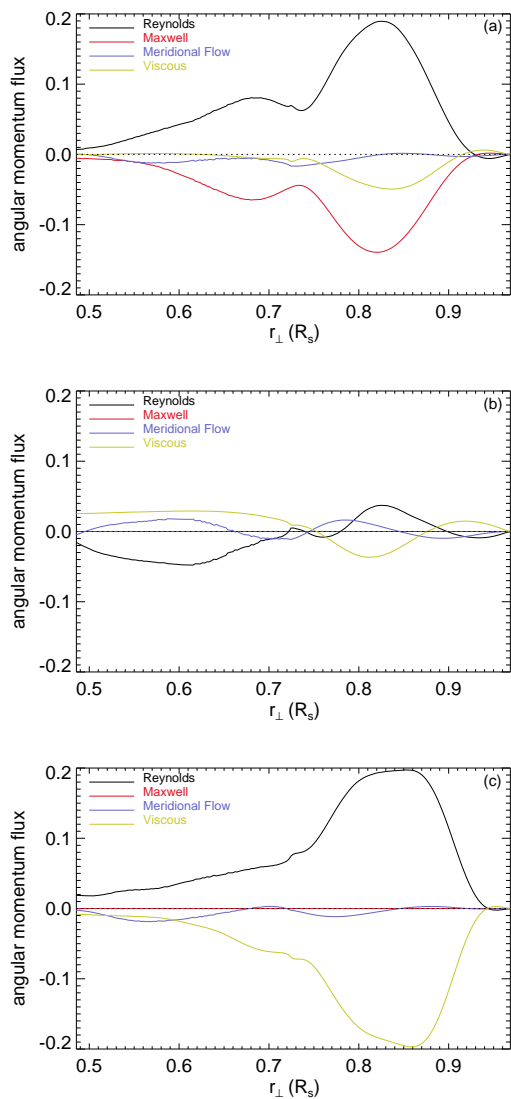
Fig. 5.— Integrated angular momentum fluxes across cylinders centered on the rotation axis as a function of the radial distance $r_\perp$ from the rotation axis for respectively the dynamo case (a), the corresponding HD case (b), and the HVHD case (c). The $r_\perp$ of the tangent cylinder of the base of the CZ is $0.722 R_s$
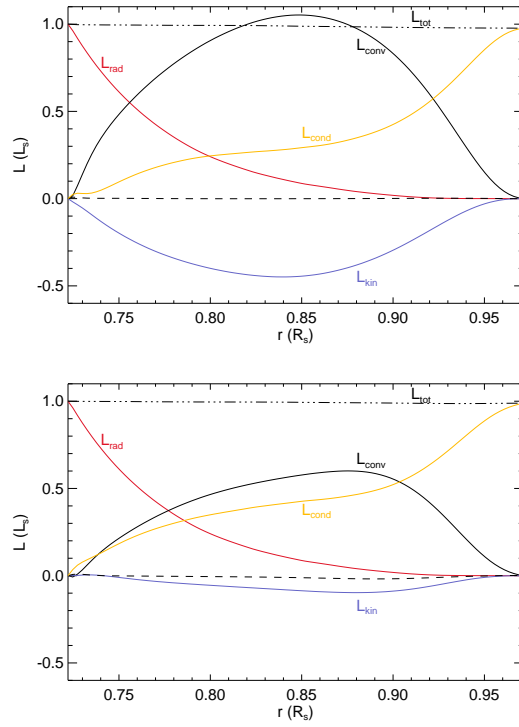
Fig. 6.— Same as Figure 2(b) but for the corresponding HD case (upper panel) and the HVHD case (lower panel).
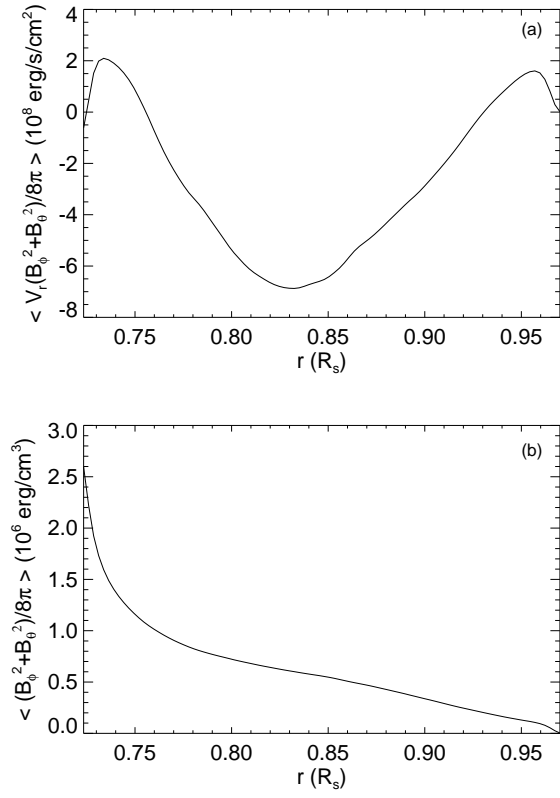
Fig. 7.— (a) Advective flux of the horizontal magnetic field energy, and (b) the distribution of horizontal magnetic field energy as a function of depth.
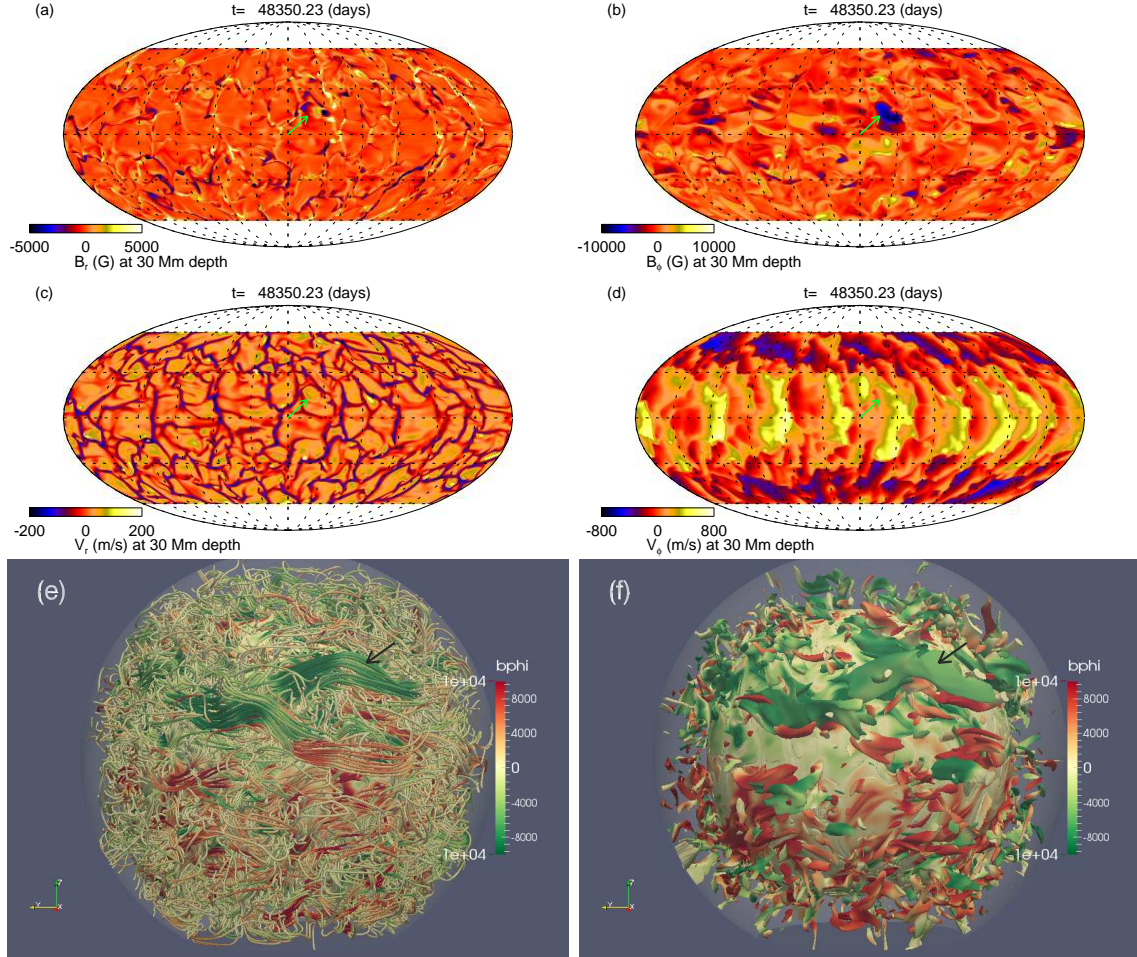
Fig. 8.— Panels (a), (b), (c), and (d) show respectively snapshots of $B_r$, $B_\phi$, $v_r$, and $v_\phi$ at a shell slice at the depth of 30 Mm below the photosphere, displayed on the full sphere in Mollweide projection. A movie showing the evolution of $B_r$, $B_\phi$, $v_r$ at the 30 Mm depth, and also $B_\phi$ at a depth near the bottom of the CZ, over a period of about 13 days centered around the time instant shown in this Figure is also available in the electronic version. Panels (e) and (f) show respectively 3D views of the magnetic field lines and the equipartition field iso-surfaces of $v_a/v_{\mathrm{rms}} = 1$ with $v_a$ being the Alfvén speed and $v_{\mathrm{rms}}$ being the r.m.s. convective velocity for the corresponding depth.
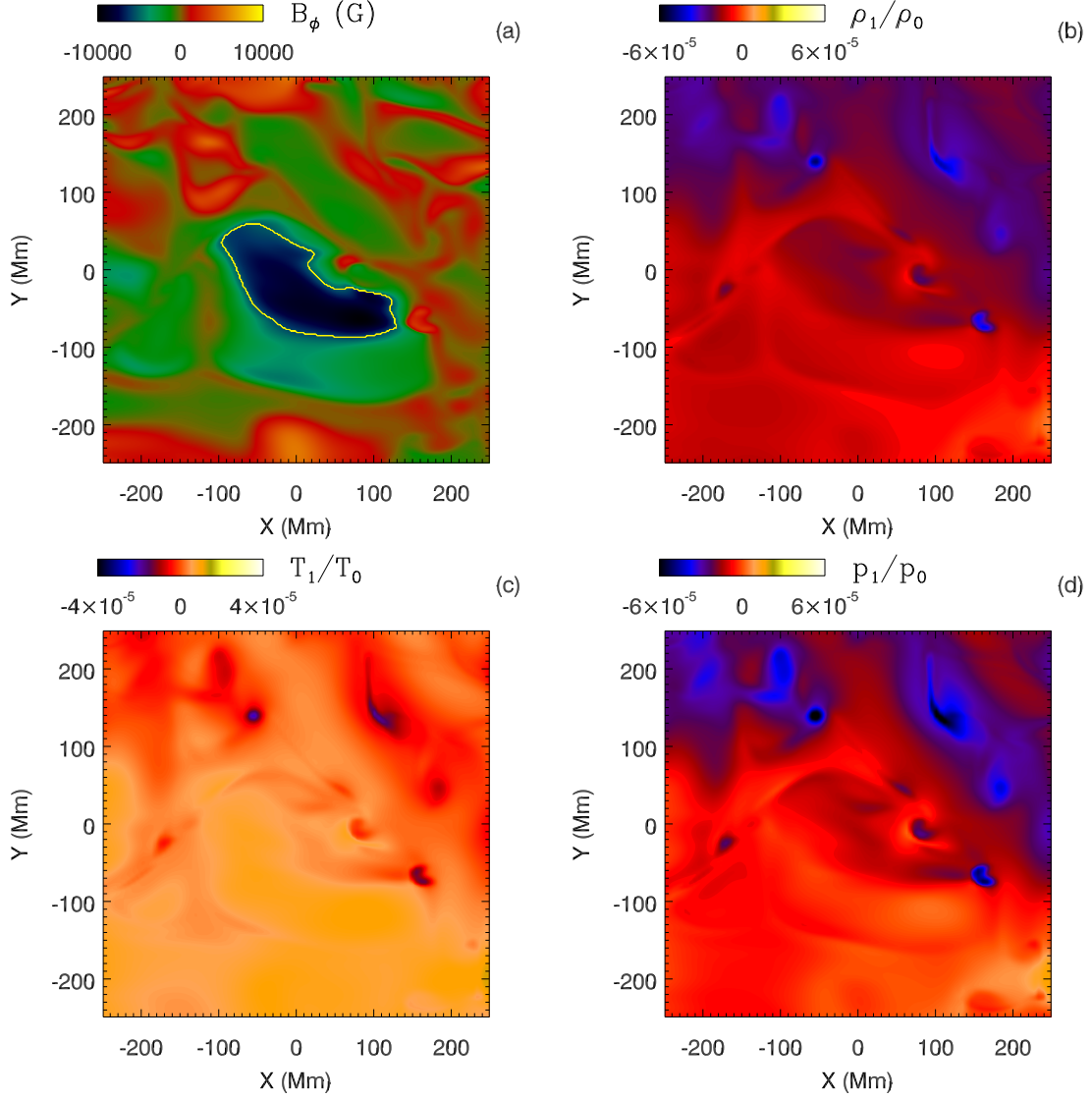
Fig. 9.— Zoomed in view centered on the emerging region on the horizontal surface at the same depth (30 Mm) as shown in Figure 8 with (a) showing $B_\phi$ and a yellow contour marking the emerging region where $B_\phi < -5000$ G and the ratio of the Alfvén speed over the r.m.s. convective speed $v_a/v_{\rm rms} > 1$, (b) showing density change $\rho_1$ relative to the reference state $\rho_0$ at that height, (c) showing temperature change $T_1$ relative to the reference state $T_0$, and (d) showing pressure change $p_1$ relative to the reference state $p_0$.
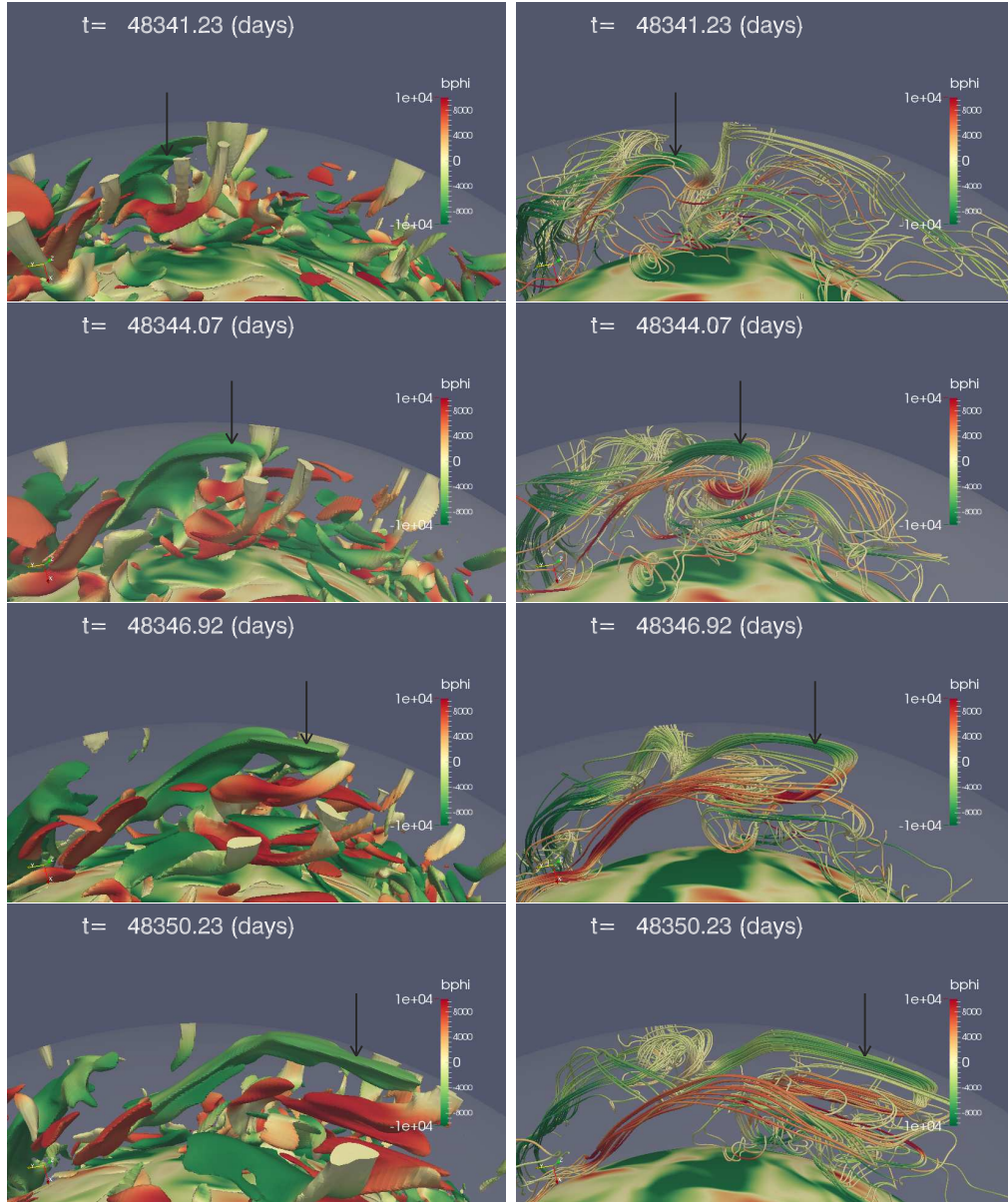
Fig. 10.— Left column images show iso-volumes of super-equipartition fields (where $v_a/v_{\mathrm{rms}} > 1$) for a period of 9 days prior to the time of the flux emergence event shown in Figure 8, with the arrow marking the evolution of the emerging flux bundle that produces the flux emergence event shown in Figure 8. Right column images show representative field lines traced from points in the iso-volume corresponding to the emerging flux bundle.
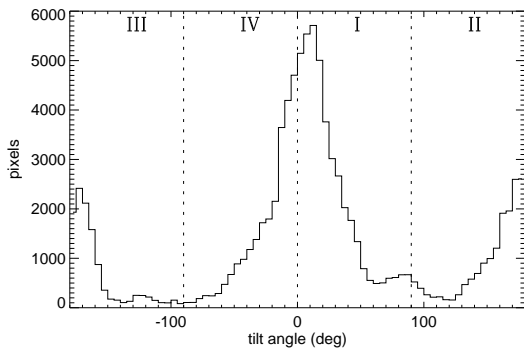
Fig. 11.— Distribution of the tilt angles of the horizontal field vectors in strong emerging field areas at 30 Mm depth. See text about the tilt angle quadrants I, II, III, and IV.